# Emergence of electron coherence and two-color all-optical switching in $MoS_2$ based on spatial self-phase modulation

Yanling Wu, Qiong Wu, Fei Sun, Cai Cheng, Sheng Meng[1], and Jimin Zhao[1]

Beijing National Laboratory for Condensed Matter Physics and Institute of Physics, Chinese Academy of Sciences, Beijing 100190, China

Edited by Roberto Merlin, University of Michigan, Ann Arbor, Michigan, and accepted by the Editorial Board July 25, 2015 (received for review March 11, 2015)

**Generating electron coherence in quantum materials is essential in optimal control of many-body interactions and correlations. In a multidomain system this signifies nonlocal coherence and emergence of collective phenomena, particularly in layered 2D quantum materials possessing novel electronic structures and high carrier mobilities. Here we report nonlocal ac electron coherence induced in dispersed $MoS_2$ flake domains, using coherent spatial self-phase modulation (SSPM). The gap-dependent nonlinear dielectric susceptibility $\chi^{(3)}$ measured is surprisingly large, where direct interband transition and two-photon SSPM are responsible for excitations above and below the bandgap, respectively. A wind-chime model is proposed to account for the emergence of the ac electron coherence. Furthermore, all-optical switching is achieved based on SSPM, especially with two-color intraband coherence, demonstrating that electron coherence generation is a ubiquitous property of layered quantum materials.**

electron coherence | transition metal dichalcogenide | self-phase modulation | optical switching | emergent phenomena

Recently 2D layered quantum materials have attracted tremendous interest since the discovery of graphene a decade ago (1). Various layered materials, ranging from boron nitride sheets to transition metal dichalcogenides and from topological insulators to high-temperature superconductors, have been intensively investigated (2–11). Strict 2D atomic crystals can now be produced at a macroscopic scale, using a variety of methods (11, 12). Among them molybdenum disulfide ($MoS_2$) and related layered quantum materials are particularly interesting due to their novel optical properties and potential valleytronics applications (4, 5, 8, 9) at a thickness of monolayer and few layers (2, 10, 13). Layered materials share common physical properties rooted in their ubiquitous 2D quantum nature, for which achieving pure coherence among electrons (lattices) is of particular interest (14–19). The presence of multiple domains is ubiquitous in many known 2D quantum materials, ranging from stripe-order cuprate superconductors to polycrystalline strongly correlated systems. For example, phase locking between different layers of stripe orders is crucial for enhancing the superconducting phase in layered high-temperature superconductors (20, 21).

In this work we demonstrate unambiguously that nonlocal and intraband ac electron coherence, of which the electronic wave function oscillates at an optical frequency of $10^{14}$ Hz, can be generated in separate $MoS_2$ flakes, using spatial self-phase modulation (SSPM). The SSPM is a coherent third-order nonlinear optical process systematically investigated decades ago (22), where the nonlinear optical susceptibility $\chi^{(3)}$ is uniquely determined by the laser-intensity-dependent refractive index $n = n_0 + n_2 I$, where $n_0$ and $n_2$ are linear and nonlinear refractive indexes, respectively. If this effect is strong enough in a material, the phenomenon of self-focusing can be directly observed. The SSPM is also frequently referred to as the optical Kerr effect or the ac Kerr effect (note the difference from the regular Kerr effect). It is parallel to the other third-order nonlinear optical processes, such as third harmonic generation (THG) and four-wave mixing (FWM).

Our investigations show that gap-dependent SSPM is a general method for inducing electron coherence in 2D layered materials. Monolayer and few-layer $MoS_2$ (and other similar layered materials) have finite bandgaps, which lift the obstacle to versatile electronic and optical applications (2, 23, 24). Because SSPM using below-gap photons has not been reported, $MoS_2$ provides an ideal test platform for observing SSPM in finite-bandgap materials. A model has been developed to account for the coherence emergence process and theoretical calculations have been carried out to unravel the underlying mechanism. Moreover, we demonstrate all-optical switching based on SSPM, which employs intraband electron coherence. This optical switch has multiple advantages, including weak-control-strong performance, cascade-possible, and high-contrast two-color switching.

## Results and Discussion

Fig. 1 displays the experimental setup and typical SSPM patterns obtained from the flake domains of $MoS_2$ in a suspension (*Methods*). It can be seen from Fig. 1*B* that the sample is mainly composed of $MoS_2$ flakes with a thickness of $30 \sim 55$ layers. In Fig. 1 *D–F* we show the SSPM patterns obtained using 400-nm ultrafast laser pulses, 532-nm continuous wave (cw) laser beams, and 800-nm ultrafast laser pulses, respectively. The SSPM is a nonlinear optical process in that the phase (rather than the intensity) of the output beam depends on the input intensity (*Methods*).

### Significance

**Generating electron coherence is nontrivial in that most sophisticated electronic experimental methods are noncoherent or cannot be used to induce and detect collective states. By using coherent spatial self-phase modulation (SSPM) (a nonlinear optical property) we observed the emergence of electron coherence in a gapped quantum material, $MoS_2$. By observing gap-dependent SSPM we discovered that it is a ubiquitous property of two-dimensional layered quantum materials. Furthermore, we demonstrate that this ac electron coherence can be harnessed to realize two-color all-optical switching with superb performance.**

Author contributions: J.Z. designed research; Y.W., Q.W., F.S., and J.Z. performed research; C.C. and S.M. obtained theoretical absorption; Q.W. and J.Z. derived wind chime model; Y.W., S.M., and J.Z. analyzed data; and S.M. and J.Z. wrote the paper.

The authors declare no conflict of interest.

This article is a PNAS Direct Submission. R.M. is a guest editor invited by the Editorial Board.

Freely available online through the PNAS open access option.

[1]To whom correspondence may be addressed. Email: jmzhao@iphy.ac.cn or smeng@iphy.ac.cn.

This article contains supporting information online at www.pnas.org/lookup/suppl/doi:10.1073/pnas.1504920112/-/DCSupplemental.

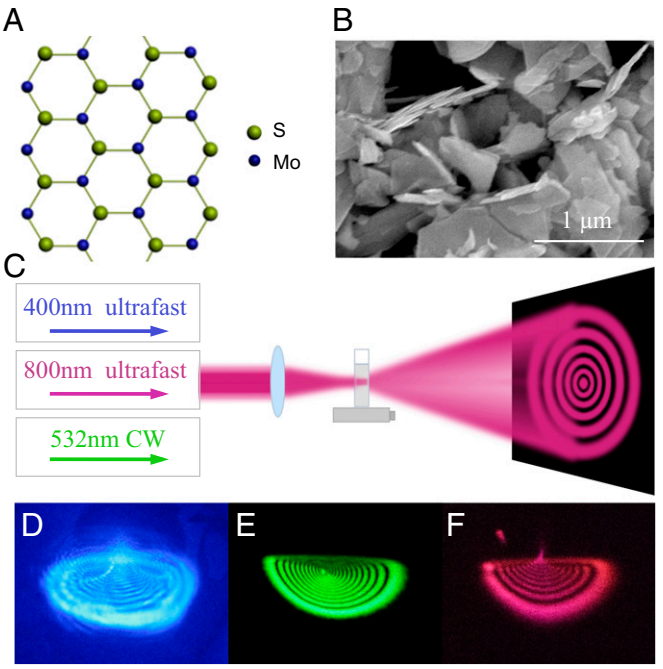


**Fig. 1.** (*A*) Schematic lattice structure of $MoS_2$. (*B*) Scanning electron microscopy image of the $MoS_2$ flakes. (*C*) Schematic experimental setup. (*D–F*) The SSPM patterns generated using 400-nm, 532-nm, and 800-nm laser beams, respectively.

To unambiguously verify that we have observed SSPM, we performed intensity-dependence measurements. Fig. 2 shows that the number of rings $N$ increases nearly linearly with the laser intensity, until the saturation is reached. By this linear dependence the optical nonlinear coefficient $n_2$, hence $\chi^{(3)}$, can be obtained directly (Fig. 2 and *Methods*). Because nearly all of the light is diffracted off the incidence direction and the Rayleigh scattering is low, ideally it is a purely coherent third-order nonlinear optical process. This pure coherence must originate from the coherence within the sample—the electron coherence, where the electronic wave function preserves a definite phase (see discussion below). In the case that photoexcited carriers become out of phase due to collisions, impurity scatterings, and boundary reflections, they reassume their coherence transiently (at a timescale of femtoseconds) under the external light pulse.

Next we consider nonlocal electron coherence. In our sample, each flake is a domain. Charge carriers in any form (including photocarriers, excitons, free electron–hole pairs, and intrinsic electrons and holes) in different and the same domains are initially completely out of phase. Besides, each domain has an arbitrary orientation. Upon light interaction, photoinduced quasiparticles interact with the electric field (Fig. 3*A*) and assume its local phases.

We propose a wind-chime model to describe the emergence of electron coherence from the nonlocal domains driven by SSPM (Fig. 3*A*). Initially there exists an arbitrary orientation angle $\theta$ between a $MoS_2$ flake (thus the electrical polarization it contains) and the electric field. Due to energy relaxation, the electric field reorients the flakes so that each domain contains an axis parallel to the polarization of the external field, as if each domain is "hung" by a vertical "thread." This image mimics that of a wind chime (Fig. 3*A*). Once the wind chime is formed, the electron coherence is completely set up within and among each of the different domains. This scenario depicts the emergence of nonlocal electron coherence as a complex collective behavior.

We first show that the model is reasonable. Assuming a circular disk shape for the $MoS_2$ flake domains, we derived (*SI Text, section S1*) that the rotation torque generated by the laser pulse $\mathcal{M} = \int |\boldsymbol{P}\times\boldsymbol{E}|\,dV$ has a magnitude of

$$\mathcal{M} = \frac{1}{4}\sin 2\theta\,\frac{(\varepsilon_r - 1)}{\varepsilon_r}\,\varepsilon_0 E_0^2 \pi R^2 h e^{-\left(2(ct-z)^2/c^2\tau^2\right)}, \qquad [1]$$

where $R$ is the disk radius, $h$ is the disk thickness, and $\tau$ is the pulse width. Taking the Newton fluid with constant viscosity coefficient $\eta$ and linear velocity $v$ at the interface, the rotation torque $\mathcal{V}$ due to the viscous force is

$$\mathcal{V} = \eta \int_0^{\pi} \frac{dv}{dr}(R\sin\varphi)(\xi\cdot 2\pi R\sin\varphi)(Rd\varphi) = \pi\eta\Omega\xi R^3, \qquad [2]$$

where $\Omega$ is the rotation velocity and $\xi$ is the portion of the fluid globe that is rotating together with the disk. Hence the rotation angle accumulated due to each single light pulse is (*SI Text, section S1*)

$$\delta\theta = \int_0^T \Omega\,dt \approx \int_0^{\infty} \Omega_0 e^{-\left(\pi\eta\xi R^3/\left(J_{MoS_2}+J_{Solution}\right)\right)t} dt = \frac{(\varepsilon_r - 1)}{\varepsilon_r}\,\frac{2T\mathit{Ih}}{4\eta\xi Rc}\sin 2\theta, \qquad [3]$$

where $T$ is the repetition period. The time needed for the pattern formation is (*SI Text, section S1*)

$$\mathcal{T} = \frac{\varepsilon_r \pi\eta\xi Rc}{1.72(\varepsilon_r - 1)\mathit{Ih}} = 0.3\ s, \qquad [4]$$

where we have used the values $\varepsilon_r = 3.33$ for $MoS_2$, $\eta = 3.2\times10^{-4}$ Pa•s for acetone, $R \sim 1$ μm, $h \sim 10$ nm, $I = 250$ W/cm$^2$, and $\xi \sim 0.03$ in our experiment. As a result, $\mathcal{T}$ does not depend on $T$. Thus, for both pulsed and cw excitations the results are identical, which has been verified in our experiment. To compare with the experiment, we recorded the formation processes of the ring patterns (see snapshots in Fig. 3 *B* and *C*). The ring number and diameter both increase monotonously with time until the maximum is reached after 0.20 s. This compares well with the predicted value by the wind-chime model. Thus, the observed

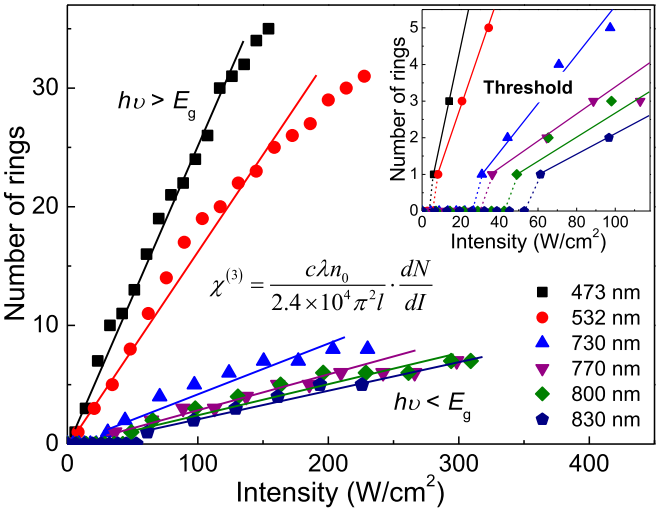


**Fig. 2.** Intensity dependence of ring numbers and bandgap dependence of $\chi^{(3)}$. The slopes directly illustrate the nonlinear coefficients $\chi^{(3)}$. The solid lines are guides to the eye. (*Inset*) The thresholds to observe the SSPM patterns at different photon energies.

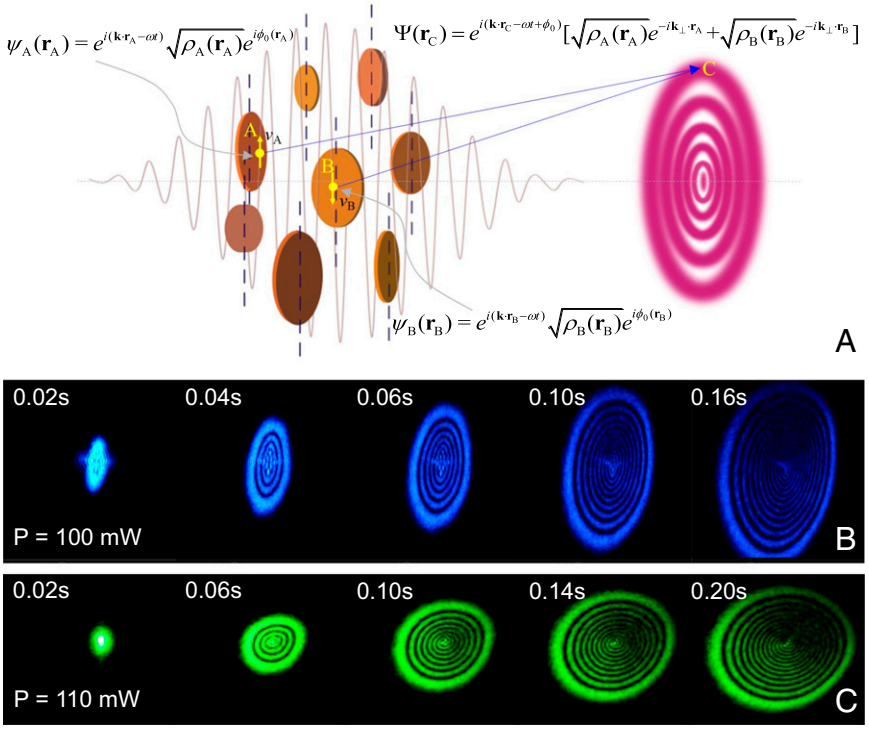


**Fig. 3.** Wind-chime model and the emergence of electron coherence. (*A*, *Left*) Collective response of the $MoS_2$ flakes to the laser beam electric field, being aligned to form a "wind chime." (*A*, *Right*) SSPM pattern formed. (*B* and *C*) Snapshots of the pattern formation at 473-nm and 532-nm laser beam excitations, respectively. The whole process takes ~0.20 s, which is consistent with the wind-chime model prediction (main text).

time for the ring formation is a strong experimental support to the wind-chime model.

We then discuss the emergence of the ac electron coherence. Writing the electronic wave function at $\mathbf{r}_A$ as $\psi_A(\mathbf{r}_A) = \sqrt{\rho_A(\mathbf{r}_A)}e^{i\phi(\mathbf{r}_A)}$, with $\psi_A^*(\mathbf{r}_A)\cdot\psi_A(\mathbf{r}_A) = \rho_A(\mathbf{r}_A)$ being the local electron density, the phase $\phi(\mathbf{r}_A) = \mathbf{k}\cdot\mathbf{r}_A - \omega t + \phi_0(\mathbf{r}_A)$ of the electronic wave function is completely determined by the external light field (Fig. 3*A*). The wave function oscillates at a frequency of $\sim 10^{14}$ Hz (i.e., optical frequency). Classically, this is a forced oscillation, where electrons have to assume the enforced local phase by the external field, even surviving scatterings and collisions. Here $\phi_0(\mathbf{r}_A)$ represents the phase lag in response to the external field. It is not the initial random phase, which is wiped off by dissipation. The same applies to the electronic wave functions at $\mathbf{r}_B$ in a different (or the same) flake. Because the two wave functions are both coherent with the light wave, they are coherent to each other too. This is a dynamic or ac electron coherence, which is different from the commonly known steady-state or dc electron coherence in transport measurements. The electrons do not move far away from their equilibrium positions. After the wind-chime formation the electron coherence becomes stronger because more electrons get correlated and fewer collisions get involved, owing to the aligned geometry. At the far field, the intensity is $I(\mathbf{r}_C) = E^*(\mathbf{r}_C)\cdot E(\mathbf{r}_C)$, where $E(\mathbf{r}_C)$ is the electric field of the light wave at $\mathbf{r}_C$. It becomes $E(\mathbf{r}_C) = \varsigma(\chi^{(3)})\Psi(\mathbf{r}_C)$, with $\Psi(\mathbf{r}_C) = e^{i(\mathbf{k}\cdot\mathbf{r}_C-\omega t+\phi_0)}[\sqrt{\rho_A(\mathbf{r}_A)}e^{-i\mathbf{k}_\perp\cdot\mathbf{r}_A} + \sqrt{\rho_B(\mathbf{r}_B)}e^{-i\mathbf{k}_\perp\cdot\mathbf{r}_B}]$ being the optical phase except for a normalization factor. Here $k_\perp = d\Delta\phi/dr$ is the wavevector generated due to the nonlinear response term of $n_2$ (*Methods*). The exact coefficient $\varsigma(\chi^{(3)})$ is determined by the optical nonlinearity $\chi^{(3)}$, which is comprehensively determined by the carrier properties in the material.

We found that SSPM can be used to measure easily the $\chi^{(3)}_{\text{onelayer}}$ value for many of the layered quantum materials (we have also observed SSPM in dispersion of $MoSe_2$ flakes and obtained the $\chi^{(3)}$ value). In other coherent methods (e.g., THG or FWM), the signal is much weaker than the input beam (25). Instead, in SSPM the diffracted beam is strong, owing to the intrinsic electron coherence. Significantly, SSPM can be used to measure $\chi^{(3)}$ from near IR to UV, compared with THG working only for the region where the 3 $\omega$ signal can be easily detected. This is essential for materials with a relatively large gap. In this sense we have found a powerful and ubiquitous (in some cases unique) way to measure $\chi^{(3)}$ for many of the 2D gapped quantum materials.

To quantitatively investigate the gap-dependent property, we obtained $\chi^{(3)}$ values for excitations at multiple wavelengths (Fig. 4*A*). For example $\chi^{(3)}_{\text{onelayer}}$ at 532 nm is $1.6\times10^{-9}$ electrostatic units (e.s.u.) (i.e., $2.23\times10^{-17}$ $m^2/V^2$; *Methods*), which is orders of magnitude larger than that of conventional semiconductors, owing to the high carrier density and mobility in 2D layered materials. In parallel we calculated the absorption as a function of wavelength for few-layer $MoS_2$, where the dipole transition is proportional to the occupation probabilities of valence and conduction bands. As shown in Fig. 4*A*, the experimental results and theoretical calculations compare well. A sharp change in $\chi^{(3)}$ and threshold values can be seen at 1.72 eV (722 nm), which is exactly the gap value of $MoS_2$. This gap-dependent property is a manifestation of the electronic band structure of $MoS_2$. Thus, SSPM can be used to investigate band structures of layered quantum materials and can be conveniently compared with other experimental methods such as absorption and photoluminescence. The SSPM method applies especially to those materials where large single crystals are not available and absorption is hard to measure.

In Fig. 4*A* the experimental results compare well with the calculated absorption along *x* and *y*, but not that along the *z* direction (*SI Text, section S2*). This is strong evidence that, in our experiment, light propagation is perpendicular to the *x* or *y* but not the *z* axis, which confirms the validity of the wind-chime model. Note that this is an even stronger restriction than the wind-chime model.

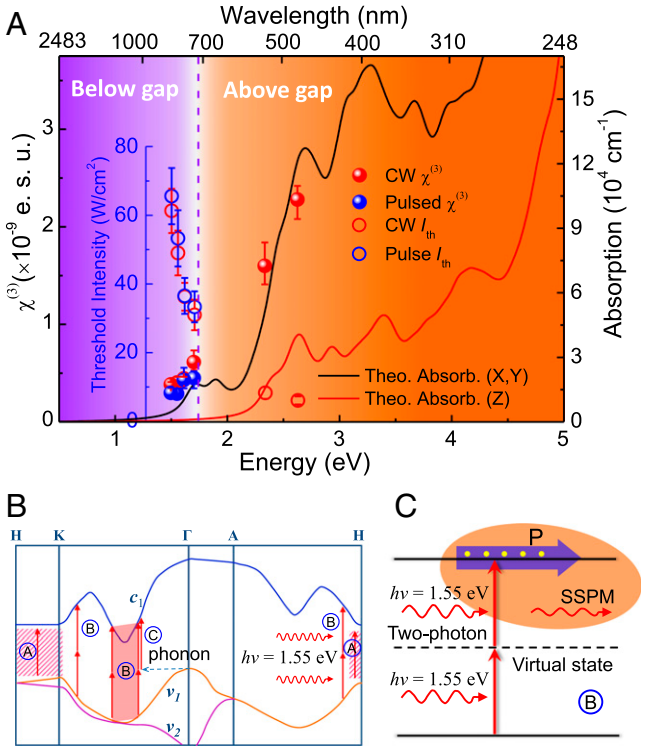


**Fig. 4.** Bandgap-dependent $\chi^{(3)}$ and $I_{th}$ and the SSPM mechanisms. (*A*) Bandgap dependence of $\chi^{(3)}$ (solid spheres) and $I_{th}$ (open circles) for ultrafast (blue) and cw (red) excitations, respectively. The calculated photoabsorption spectrum of $MoS_2$ is also shown (black and red curves) for comparison. The below-gap (purple) and above-gap (orange) regions are marked. (*B*) Scenarios of the SSPM formation mechanisms: Ⓐ Single-photon absorption-induced SSPM; Ⓑ two-photon absorption-induced SSPM; Ⓒ indirect-bandgap phonon-assisted SSPM. The bandgap structure is adopted from ref. 2. (*C*) Two-photon absorption leads to SSPM of the fundamental beam.

Considering the plasmonic interaction due to free carriers (26), it is indeed possible that the collective behavior leads to a "frozen" wind chime, where all domains become parallel to each other and perpendicular to the direction of laser propagation. The gap-dependent nature displayed in Fig. 4 shows again that SSPM is mainly due to the various charge carriers.

The below-gap SSPM has never been reported before. Three mechanisms might be responsible for it (Fig. 4 *B* and *C*): Ⓐ single-photon SSPM with Fermi distribution smearing, Ⓑ two-photon SSPM, and Ⓒ phonon-assisted indirect-gap SSPM. For Ⓐ, it can be seen that Fermi smearing relevant for significant photoabsorption occurs only at zones near the H and K points in momentum space. For Ⓑ, the carriers generated through two-photon absorption build up an electrical polarization, which diffracts not only those photons above the gap, but also those below the gap (Fig. 4*B*). As such, even though it is a two-photon nonlinear process, one expects a linear power dependence relation because the change in refractive index is proportional to the light intensity *I*. Heuristically, the excited carriers diffract both excitation photons (i.e., two output photons). In comparison there is only one output photon in second harmonic generation and two-photon photoluminescence. Two-photon SSPM is the most likely mechanism responsible for below-gap SSPM. For Ⓒ, the indirect gap photon excitation requires assistant phonon injection (Fig. 4*C*), which usually has a very small probability. In-gap defect states are relatively sparse (resonant in-gap states are more sparse) and localized (whereby charge carriers cannot move freely and scattering occurs frequently, which ruins the acquired uniform phase), so they are unlikely a major reason for SSPM.

We further demonstrate that, in forming SSPM, free carriers generated by photons at one wavelength can diffract photons at another wavelength, as if they were generated by the latter photons. The experimental setup is illustrated in Fig. 5*C*, which demonstrates a two-color (473 nm and 532 nm) SSPM. When we fix the power of one beam (even below threshold) and increase that of the other, the ring number and diameter for each beam both increase simultaneously. The brightness decreases, with the total intensity remaining unchanged, and energy conservation is preserved (Fig. 5*D*). In Fig. 5*B* the ring number of the 473-nm pattern exhibits linear dependence on the sum of the two beam powers, although the intensity of the 473-nm beam is fixed. The same is true for the 532-nm ring (*SI Text, section S3*). Once the coherence is correlated, each beam experiences the SSPM—as if the free carriers are created by the beam itself. Fig. 5*A* is an overall illustration of this property. This indistinguishability helps explain why in two-photon SSPM one can still have linear dependence and still obtain a relatively large $\chi^{(3)}$.

Significantly, our experiment is to our knowledge the first demonstration of all-optical switching based on SSPM. Because the switching beam is controlling the phase of the other one, a small change in intensity will result in the shift of the strong signal pattern in real space, where a detector is placed. The detector can be made to detect the whole rings. Thus, a weaker beam can switch on and off a stronger beam (27, 28). Quantitatively taking the intensity of the signal beam (strong beam) at 473 nm to be $I_{strong} = 120$ W/cm$^2$, the intensity of the control beam (weak beam) at 532 nm needs only to be $I_{weak} = 2.0$ W/cm$^2$ to change the phase of the strong beam by $\pi$ (i.e., $\Delta N = 0.5$, Fig. 2). Hence to make an all-optical switch with full contrast ratio, $I_{weak}$:$I_{strong}$ = 1:60. This is characteristic of weak-control–strong all-optical switching, which is apparently cascade possible (27, 28).

It is interesting that in the experiment intraband electron coherence has been correlated between photocarriers of 473-nm and 532-nm excitations. We note that similar coherence is also induced among the holes, the excitons, and the free electron–hole pairs. The two-color switching can further enable high-contrast-ratio operations, because in two-color operation optical filters can be used to block the signal beam. Two-color switching also makes it possible for multichannel mixed switching and thus enables very broad-band optoelectronic devices. We leave additional details of the SSPM-based all-optical switching to future investigations. In summary, our experiment demonstrates an all-optical switching based on SSPM, with the advantages including a weak-control–strong, cascade-possible, high-contrast-ratio, room-temperature device; broadband functioning; condensed state; and particularly broad-band-accessible quantum materials.

## Conclusions

In conclusion, nonlocal ac electron coherence among different flake domains of $MoS_2$ has been optically correlated based on SSPM. A wind-chime model is proposed to account for this emergent collective behavior, which is verified by experimental observation of the pattern formation time. Significantly, gap-dependent SSPM has been observed, where the $\chi^{(3)}$ value and the threshold $I_{th}$ both show abrupt changes across the $MoS_2$ bandgap. Mechanisms including two-photon SSPM have been discussed. Furthermore, we have experimentally demonstrated all-optical switching based on SSPM, which employs the intraband electron coherence. Our investigation signifies a ubiquitous property of 2D layered quantum materials and extends their potentials in optoelectronic applications by realizing all-optical switching.

## Methods

**Ultrafast and cw Experiment of SSPM in $MoS_2$.** Multiple ultrafast and cw laser beams were used to investigate the SSPM from suspended $MoS_2$ flakes. In the ultrafast experiment, 800-nm light pulses of 200-fs pulse width and 80-MHz repetition rate were focused onto the sample. The solvent is acetone and the container is a 1-cm-thick cuvette. The distance between the focusing lens

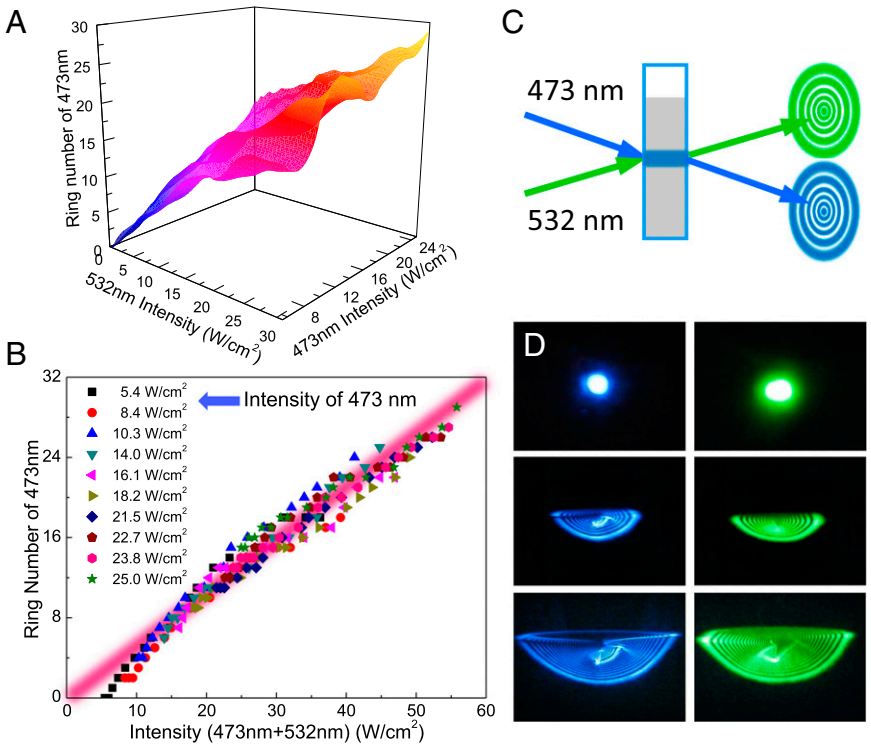


**Fig. 5.** All-optical switching based on SSPM. (*A* and *B*) Dependence of the 473-nm beam ring number on the sum intensity. (*C*) Schematic of the switch. (*D*) Generating the 473-nm pattern by increasing the 532-nm beam intensity. Both ring numbers (and diameters) increase simultaneously, with fixed 473-nm intensity below threshold.

($f = 200$ mm) and the center of the cuvette is kept fixed at 150 mm. The beam spot size after focusing is 0.2 mm for the $1/e^2$ intensity radius. In the cw experiment, single transverse-mode 532-nm and 473-nm laser beams were used instead, having a similar beam spot size on the sample. The relation between the fringe thickness and the flake concentration is investigated and discussed in *SI Text, section S4*. Micrometer-sized powder of $MoS_2$ crystals (LSKYD, www.kydmaterials.com/en/index.php) was added into the solvent and then ultrasonicated for 30 min before the measurement. The optimum concentration is 0.14 g/L (i.e., $8.5 \times 10^{-4}$ mol/L). From our Raman and absorption characterization there are very few monolayer $MoS_2$ flakes in our sample (*SI Text, section S5*). From Fig. 1*B*, it can be seen that our sample is mainly composed of $MoS_2$ flakes with a thickness of $30 \sim 55$ layers. Being different from the linear optical phenomena of Newton's rings, the SSPM pattern has a finite number of fringes and the thickest fringe has the largest diameter. The critical proof of observing a SSPM pattern is that the number of rings, *N*, increases linearly with the input laser intensity.

**Fundamentals of SSPM and the Calculation of the $\chi^{(3)}_{\text{onelayer}}$ in $MoS_2$.** The nonlinear optical response SSPM is characterized by $n = n_0 + n_2 I$, where $n_0$ and $n_2$ are the linear and nonlinear refractive indexes, respectively. Assuming a Gaussian beam, the optical phase accumulated after propagation length $l$ is $\Delta\psi(r) = (2\pi n_0/\lambda)\int_{-l/2}^{l/2} n_2 I(r,z)dz$, where $z$ is the propagation direction of the incident laser beam. Thus, we have $\Delta\psi(0) - \Delta\psi(\infty) = (2\pi n_0/\lambda)n_2 \cdot 2I \cdot l$, with $I(0, z) = 2I$. The number of rings $N$ is proportional to the phase change in the output beam ($\Delta\psi(0) - \Delta\psi(\infty) = 2\pi N$), leading to $n_2 = (\lambda/2n_0 l)(N/I)$, where $n_0 = 1.36$ and $N$ is proportional to $I$ for a nearly constant $n_2$. By the slope in Fig. 2 we can straightforwardly obtain $n_2$ from the experimental data. With $n_2 = (12\pi^2/(n_0^2 c))10^3\chi^{(3)}$ (in the SI unit) we estimate that $\chi^{(3)} = 1.44 \times 10^{-4}$ e.s.u. for the 532-nm cw laser beam excitation. The number of effective single layers, $M$, that the laser beam passes through is estimated to be about 300, using the concentration of the sample (*SI Text, section S6*). As $I_{\text{total}} \sim M^2 I_{\text{onelayer}}$, we estimate that $\chi^{(3)} = M^2\chi^{(3)}_{\text{onelayer}}$. The estimated $\chi^{(3)}_{\text{onelayer}}$ for 532 nm is $1.6 \times 10^{-9}$ e.s.u. (i.e., $2.23 \times 10^{-17}$ $m^2/V^2$).

**Conveyance of the ac Electron Coherence to the Optical Coherence.** The diffraction of the beam off the $z$ axis is due to a finite perpendicular wavevector, which is, for a Gaussian beam $\Delta\psi(r) = \Delta\psi(0)\exp(-2r^2/a^2)$, explicitly written as $k_\perp = d\Delta\psi(r)/dr = (-16\pi n_0 n_2 Il/a^2\lambda)r \cdot \exp(-2r^2/a^2)$. After the wind chime is formed, the optical coherence forming the fringes is conveyed from the electron coherence:

$$\begin{aligned}\Psi(\mathbf{r}_C) &= \left[\sqrt{\rho_A(\mathbf{r}_A)}e^{i\phi(\mathbf{r}_A)}e^{i|\mathbf{k}_z\cdot(\mathbf{r}_C-\mathbf{r}_A)|}e^{i\left[\nabla_{r_\perp}(\Delta\phi)\big|_{\mathbf{r}_A}\right]\widehat{r_\perp}\cdot(\mathbf{r}_C-\mathbf{r}_A)}\right.\\ &\quad\left.+\sqrt{\rho_B(\mathbf{r}_B)}e^{i\phi(\mathbf{r}_B)}e^{i|\mathbf{k}_z\cdot(\mathbf{r}_C-\mathbf{r}_B)|}e^{i\left[\nabla_{r_\perp}(\Delta\phi)\big|_{\mathbf{r}_B}\right]\widehat{r_\perp}\cdot(\mathbf{r}_C-\mathbf{r}_B)}+\ldots\right]\\ &= e^{i(\mathbf{k}_z\cdot\mathbf{r}_C-\omega t)}\left[\sqrt{\rho_A(\mathbf{r}_A)}e^{i\phi_0(\mathbf{r}_A)}e^{i\left[\nabla_{r_\perp}(\Delta\phi)\big|_{\mathbf{r}_A}\right]\widehat{r_\perp}\cdot(\mathbf{r}_C-\mathbf{r}_A)}\right.\\ &\quad\left.+\sqrt{\rho_B(\mathbf{r}_B)}e^{i\phi_0(\mathbf{r}_B)}e^{i\left[\nabla_{r_\perp}(\Delta\phi)\big|_{\mathbf{r}_B}\right]\widehat{r_\perp}\cdot(\mathbf{r}_C-\mathbf{r}_B)}+\ldots\right]\\ &= e^{i(\mathbf{k}\cdot\mathbf{r}_C-\omega t+\phi_0)}\left[\sqrt{\rho_A(\mathbf{r}_A)}e^{-i\,\mathbf{k}_\perp\cdot\mathbf{r}_A}+\sqrt{\rho_B(\mathbf{r}_B)}e^{-i\,\mathbf{k}_\perp\cdot\mathbf{r}_B}+\ldots\right].\end{aligned}$$

Here we have taken that $\phi_0$ is identical for $\mathbf{r}_A$ and $\mathbf{r}_B$, and only identical $\boldsymbol{k}_\perp$ can produce interference rings.

**ACKNOWLEDGMENTS.** We acknowledge useful discussion with C.-K. Shih, James Hinton, and Joseph Orenstein. This work was supported by the National Basic Research Program of China (2012CB821402 and 2012CB921403), the National Natural Science Foundation of China (11274372 and 11222431), and the External Cooperation Program of the Chinese Academy of Sciences (GJHZ1403).

1. Novoselov KS, et al. (2004) Electric field effect in atomically thin carbon films. *Science* 306(5696):666–669.
2. Mak KF, Lee C, Hone J, Shan J, Heinz TF (2010) Atomically thin $MoS_2$: A new direct-gap semiconductor. *Phys Rev Lett* 105(13):136805.
3. Xu XD, Yao W, Xiao D, Heinz TF (2014) Spin and pseudospins in layered transition metal dichalcogenides. *Nat Phys* 10(5):343–350.
4. Kim JH, et al. (2014) Ultrafast generation of pseudo-magnetic field for valley excitons in $WSe_2$ monolayers. *Science* 346(6214):1205–1208.
5. Xiao D, Liu GB, Feng W, Xu X, Yao W (2012) Coupled spin and valley physics in monolayers of $MoS_2$ and other group-VI dichalcogenides. *Phys Rev Lett* 108(19): 196802.
6. Mak KF, et al. (2013) Tightly bound trions in monolayer $MoS_2$. *Nat Mater* 12(3):207–211.
7. Jones AM, et al. (2014) Spin–layer locking effects in optical orientation of exciton spin in bilayer $WSe_2$. *Nat Phys* 10(2):130–134.
8. Zeng H, Dai J, Yao W, Xiao D, Cui X (2012) Valley polarization in $MoS_2$ monolayers by optical pumping. *Nat Nanotechnol* 7(8):490–493.

9. Xiao D, Yao W, Niu Q (2007) Valley-contrasting physics in graphene: Magnetic moment and topological transport. *Phys Rev Lett* 99(23):236809.
10. Basov DN, Fogler MM, Lanzara A, Wang F, Zhang YB (2014) Colloquium: Graphene spectroscopy. *Rev Mod Phys* 86(3):959–994.
11. Novoselov KS, et al. (2005) Two-dimensional atomic crystals. *Proc Natl Acad Sci USA* 102(30):10451–10453.
12. Coleman JN, et al. (2011) Two-dimensional nanosheets produced by liquid exfoliation of layered materials. *Science* 331(6017):568–571.
13. Fei Z, et al. (2012) Gate-tuning of graphene plasmons revealed by infrared nano-imaging. *Nature* 487(7405):82–85.
14. Wu R, et al. (2011) Purely coherent nonlinear optical response in solution dispersions of graphene sheets. *Nano Lett* 11(12):5159–5164.
15. Hendry E, Hale PJ, Moger J, Savchenko AK, Mikhailov SA (2010) Coherent nonlinear optical response of graphene. *Phys Rev Lett* 105(9):097401.
16. Singh A, et al. (2014) Coherent electronic coupling in atomically thin $MoSe_2$. *Phys Rev Lett* 112(21):216804.
17. Kumar N, et al. (2013) Third harmonic generation in graphene and few-layer graphite films. *Phys Rev B* 87(12):121406.
18. Ge S, et al. (2014) Coherent longitudinal acoustic phonon approaching THz frequency in multilayer molybdenum disulphide. *Sci Rep* 4:5722.
19. Cheng JL, Vermeulen N, Sipe JE (2014) Third order optical nonlinearity of graphene. *New J Phys* 16:053014.
20. Mankowsky R, et al. (2014) Nonlinear lattice dynamics as a basis for enhanced superconductivity in $YBa_2Cu_3O_{6.5}$. *Nature* 516(7529):71–73.
21. Berg E, et al. (2007) Dynamical layer decoupling in a stripe-ordered high-$T(_c)$ superconductor. *Phys Rev Lett* 99(12):127003.
22. Durbin SD, Arakelian SM, Shen YR (1981) Laser-induced diffraction rings from a nematic-liquid-crystal film. *Opt Lett* 6(9):411–413.
23. Kappera R, et al. (2014) Phase-engineered low-resistance contacts for ultrathin $MoS_2$ transistors. *Nat Mater* 13(12):1128–1134.
24. Sie EJ, et al. (2014) Valley-selective optical Stark effect in monolayer $WS_2$. *Nat Mater* 14(3):290–294.
25. Wang R, et al. (2014) Third-harmonic generation in ultrathin films of $MoS_2$. *ACS Appl Mater Interfaces* 6(1):314–318.
26. Bian F, et al. (2010) Laser-driven silver nanowire formation: Effect of femtosecond laser pulse polarization. *Chin Phys Lett* 27(8):088101.
27. Han XF, et al. (2008) Single-photon level ultrafast all-optical switching. *Appl Phys Lett* 92(15):151109.
28. Dawes AMC, Illing L, Clark SM, Gauthier DJ (2005) All-optical switching in rubidium vapor. *Science* 308(5722):672–674.
29. Shi H, et al. (2013) Exciton dynamics in suspended monolayer and few-layer $MoS_2$ 2D crystals. *ACS Nano* 7(2):1072–1080.
30. Lee C, et al. (2010) Anomalous lattice vibrations of single- and few-layer $MoS_2$. *ACS Nano* 4(5):2695–2700.